Effects of Newtonian and shear thinning fluid mixing on electrokinetic instability in microchannel flows with conductivity gradients

Md Mainul Islam, Seyed Mojtaba Tabarhoseini, Nicole Miller, Yu-Hsiang Lee, Aimee Sayster, Joshua B. Bostwick, Yuhao Xu, and Xiangchun Xuan*

Department of Mechanical Engineering, Clemson University, Clemson, South Carolina 29634-0921, USA

(Received 11 October 2025; accepted 23 January 2026; published 10 February 2026)

Electrokinetic instability (EKI) emerges when fluids with differing electrical conductivities interact with an applied electric field, resulting in interfacial waves that can either disrupt or enhance microfluidic processes. Previous studies on EKI have primarily focused on Newtonian fluids, though many practical applications involve the mixing of different rheological fluids. This work investigates the effects of Newtonian and shear thinning rheology mixing on EKI using a T-shaped microchannel. We find that adding xanthan gum (XG) polymer to the high-conductivity buffer results in lower threshold electric fields and higher wave speeds/amplitudes than the configuration with XG in the low-conductivity buffer. In contrast, the threshold electric fields for the configuration with XG in both buffers are in between the two rheology mixing configurations. These findings suggest the gradient of rheology interacts with that of conductivity and may itself be able to induce instability in electrokinetic flows. We also perform a scaling analysis to account for the fluid shear thinning effect on the electric Rayleigh number in terms of a power-law model. The critical values of this dimensionless number for the onset of EKI exhibit similar variations to the threshold electric field across fluid configurations and XG concentrations.

DOI: 10.1103/v4rm-zsg2

I. INTRODUCTION

Electric-field-driven flow, known as electrokinetic flow, has become a cornerstone in microfluidic applications because of its unique advantages [1,2]. Unlike pressure-driven flow, electrokinetic flow exhibits a pluglike velocity profile that minimizes shear-induced dispersion and enables precise sample handling in lab-on-a-chip systems [3–5]. This mechanism facilitates efficient fluid pumping and sample handling in microchannels without the need for mechanical components, making it ideal for applications such as biochemical analysis, point-of-care diagnostics, and particle manipulation [6–8]. However, electrokinetic flows are highly sensitive to surface and fluid properties [9–11]. Nonuniformities, such as differences in electrical conductivity and permittivity, can induce charge accumulation, resulting in localized flow disturbances if the applied electric field is above a threshold value [12,13]. These disturbances manifest as periodic or irregular interfacial waves known as electrokinetic instability (EKI) [14]. Depending on the application, EKI can either disrupt precision processes or be leveraged to enhance micromixing. In scenarios like electric field amplified sample stacking [15], electro-osmotic velocity measurement [16] and sheath focusing-based particle separation [17], EKI must be minimized to ensure the stability of interfaces [18]. Conversely, the very same instability can be utilized to significantly boost the efficiency of microfluidic mixers or reaction platforms, especially when conventional mixing is limited by low Reynolds numbers and the absence of moving parts [19–21].

*Contact author: xcxuan@clemson.edu

There have been a good number of studies on EKI in Newtonian flows with varying channel configurations and fluid properties [22–27]. In particular, the Santiago group has developed the theoretical framework for EKI in Newtonian fluids in their earlier studies [28–30]. They showed that the onset of instability is governed by an electric Rayleigh number, defined as the ratio of electroviscous velocity (an internal velocity scale driven by charge accumulation at the diffusive conductivity interface) to diffusive velocity. Over the years, several formulations of the electric Rayleigh number have been proposed for studies of electrohydrodynamic instabilities [31–35]. The primary differences among these formulations stem from the approach to scaling the electroviscous velocity. This velocity scale depends on how the charge density and viscous stresses are scaled. Some of the earliest approaches, like those by Hoburg and Melcher [31], scaled the charge density by assuming that the internally induced electric field matches the order of the applied field. On the other hand, Baygents and Baldessari [32] proposed a model where the charge density is proportional to a linear gradient in electrical conductivity. Lin *et al.* [33] found that in channels with shallow depths, the depth dimension governs viscous stresses that enhance the flow stability. Storey *et al.* [34] and Oddy and Santiago [35] incorporated this stabilizing effect by using the channel depth as the length scale for viscous stresses. Unlike Baygents and Baldessari's approach [32], these studies omitted the charge density's dependence on the strength of conductivity gradients. Chen *et al.* [28] introduced a more comprehensive framework by incorporating a nonlinear charge density scale that accounts for perturbations of electric fields within the diffusion length. They proposed the following expression of the electric Rayleigh number, Ra_e, for EKI,

$$\mathrm{Ra}_e = \frac{U_{\mathrm{ev}} h}{D} = \Gamma \frac{h}{\delta} \frac{\varepsilon E^2 d^2}{\mu D}, \tag{1}$$

where U_{ev} is the electroviscous velocity noted above, h is the half-width of the microchannel, D is the diffusivity of ions, $\Gamma = (\gamma - 1)^2/(\gamma + 1)^2$ accounts for conductivity gradients with γ representing the electrical conductivity ratio between the high- and low-conductivity fluids, δ is the diffusion length of ions, ε is the fluid permittivity, E is the magnitude of the externally applied electric field, d is the half depth of the microchannel, and μ is the fluid viscosity.

However, many real-world fluids, for example, biological samples (e.g., blood, mucus, and urine) in biomedical applications and polymer-laden solutions in chemical processing exhibit shear thinning and viscoelastic behaviors [36–42]. Such non-Newtonian fluids have also gained significant interest in electrochemical systems and electromembrane technologies [43–47]. Recent works by the Archer group [43–45] demonstrated that adding viscoelastic polymer additives to liquid electrolytes can promote an earlier transition to unsteady electroconvective flow and enhance the spatial and temporal uniformity of ion flux at the interface. Their findings offer a promising strategy to suppress dendrite growth in batteries, thereby improving overall cell performance. In a related numerical study on electroconvection in shear thinning electrolytes, Maurya *et al.* [47] found that shear thinning polymers produce smaller yet more intense vortices near ion-selective membranes than the Newtonian electrolytes, leading to enhanced ion transport. By promoting more uniform ion distributions and mitigating ion-depletion zones, their results also suggest an approach to improve the stability of electrochemical devices. These studies highlight the crucial role of fluid rheology in electroconvection and the design improvement of electrochemical systems. As the electroconvective flow is predominantly governed by the electrohydrodynamic and electrokinetic effects, it is relevant to investigate the influence of fluid rheological properties on EKI.

To date, only a small number of papers have been published in this direction. Our group reported an experimental study of EKI in viscoelastic fluids by dissolving equal weights of polyethylene oxide (PEO) polymer into the coflowing buffers with different ionic concentrations (and hence with conductivity gradients) [48]. It was observed that adding a small amount of PEO polymer reduces the threshold electric field required for instability onset while further increasing the polymer concentration reverses the trend. In a later work, Sasmal [49] developed an Oldroyd-B fluid–based numerical model to study the influence of viscoelasticity on EKI. A suppressed chaotic convection

was predicted with the increase of the Weissenberg number (the ratio of elastic to viscous forces) or polymer-to-solvent viscosity ratio. Hamid and Sasmal [50] also developed a power-law fluid–based numerical model, which predicted the threshold electric field to decrease with decreasing power-law index, i.e., increasing shear thinning effect. This prediction was later verified by an experimental study from our group on EKI in shear thinning fluids, which were prepared by adding xanthan gum (XG) polymer to both buffers [51]. In a more recent work, our group revisited EKI in viscoelastic fluids using negatively charged hyaluronic acid (HA) polymer to form Boger solutions [52], which removed the requirement of pressure pumping in our previous study with neutral PEO solutions [48]. We observed monotonically increasing threshold electric fields in higher concentration HA solutions, supporting the earlier numerical prediction by Sasmal [49].

In our paper on EKI in shear thinning XG solutions [51], we also extended the expression of electric Rayleigh number, Ra_e, from Chen *et al*. [28] to account for the effects of shear-dependent viscosity. We proposed the following expression for the critical electric Rayleigh number ratio from shear thinning to Newtonian fluids [51]:

$$\frac{\mathrm{Ra}_{e,\mathrm{cr}}}{\mathrm{Ra}_{e,\mathrm{cr},0}} = \left(\frac{\Gamma}{\Gamma_0}\right)\sqrt{\left(\frac{\mu}{\mu_0}\right)\left(\frac{U_{\mathrm{eo}}}{U_{\mathrm{eo},0}}\right)}\left(\frac{E_{\mathrm{th}}}{E_{\mathrm{th},0}}\right)^2, \tag{2}$$

where $\mathrm{Ra}_{e,\mathrm{cr}}$ is the critical value of Ra_e in Eq. (1) for the onset of EKI at the threshold electric field, E_{th}, the subscript 0 denotes parameters corresponding to the Newtonian solvent, and U_{eo} is the electro-osmotic velocity. The obtained Rayleigh ratio in Eq. (2) was found to decrease in higher concentration XG solutions, indicating the enhancement effect of fluid shear thinning on EKI. It was also used to analyze our recent experimental results on EKI in viscoelastic HA solutions and was found to increase with increasing HA concentration [52]. This trend suggests the suppression effect of fluid elasticity on EKI, in contrast to that of shear thinning [51]. Both these rheological effects on EKI are qualitatively consistent with the earlier numerical predictions from Sasmal and co-worker [49,50]. However, the formulation in Eq. (2) incorporated only the effects of fluid viscosity on the diffusivity and diffusion length of ions. It did not consider fluid-rheology-induced modifications in viscous stresses and hence the electric Rayleigh number.

In this work, we revise the scaling analysis of Chen *et al*. [28] to incorporate the effect of shear thinning on viscous stresses and develop an expression of electric Rayleigh number for EKI in power-law fluids. Further, we investigate EKI in the Newtonian and shear thinning rheology mixing setups using a T-shaped microchannel. By varying the placement of XG polymer relative to the buffer concentration (that is, adding XG polymer to either the high- or low-concentration buffer), we examine how the direction of rheology gradients interacts with that of conductivity gradients to influence EKI behavior. This kind of rheological blend is common in applications such as food mixing [53], drug delivery [54,55], or mixing biological and synthetic solutions [56,57]. The experimental and theoretical findings from the two types of rheology mixing configurations are compared with those from a purely Newtonian configuration and as well our previous study, where XG polymer was added to both buffer solutions, forming a homogeneous rheology configuration [51]. Overall, this study provides a complete picture of how fluid configuration and shear thinning rheology affect EKI in microchannel flows.

II. THEORETICAL FORMULATION

A. Electric Rayleigh number in power-law fluids

To model EKI in high-aspect-ratio experimental systems ($d/h \ll 1$), Chen *et al*. [28] developed linearized thin-layer governing equations. They identified an electric Rayleigh number, i.e., Ra_e in Eq. (1), that governs the onset of convective EKI in Newtonian fluids. In this section we extend Chen *et al*.'s formulation of Ra_e to incorporate the shear thinning effects of power-law fluids. The

following scaling is adopted in the analysis,

$$x,\ y\ \sim\ h,\ z\ \sim\ d,\ u_0\ \sim\ U_{\mathrm{eo}},\ v_0, w_0 = 0,\ u', v'\ \sim\ U_{\mathrm{ev}},\ w' = U_{\mathrm{ev}} d/h \tag{3}$$

where x, y, and z are the coordinates along the length, width, and depth direction of the main branch, respectively, u_0, v_0, and w_0 are the corresponding electro-osmotic velocity components at the base state, and the superscripts '′' denote the perturbed state. Based on the arguments presented by Chen *et al*. [28], we used the electroviscous velocity, U_{ev}, as the perturbation velocity (u', v', w') scale due to EKI, and the electro-osmotic velocity, U_{eo}, to scale the base electro-osmotic flow.

The dynamic viscosity of power-law fluids is given by [58],

$$\mu = K(\dot{\gamma})^{n-1}, \tag{4}$$

where K is the flow consistency index and n is the flow behavior index or power-law index, and $\dot{\gamma}$ is the shear rate defined as,

$$\dot{\gamma} = \sqrt{2\mathbf{S} : \mathbf{S}}, \tag{5}$$

with $\mathbf{S}$ being the strain rate tensor. In thin-layer systems, the dominant strain rate components come from the depth direction (i.e., z direction) and scale as follows:

$$S_{xz} = S_{zx} = \frac{1}{2}\left(\frac{\partial u}{\partial z} + \frac{\partial w}{\partial x}\right) = \frac{1}{2}\left\{\frac{\partial u_0}{\partial z} + \frac{\partial u'}{\partial z} + \frac{\partial w'}{\partial x}\right\} \sim \frac{1}{2}\left(\frac{U_{\mathrm{ev}}}{d} + \frac{U_{\mathrm{ev}}}{d}\frac{d^2}{h^2}\right) \sim \mathrm{O}\left(\frac{U_{\mathrm{ev}}}{d}\right). \tag{6}$$

Similarly,

$$S_{yz} = S_{zy} = \frac{1}{2}\left(\frac{\partial v}{\partial z} + \frac{\partial w}{\partial y}\right) \sim \mathrm{O}\left(\frac{U_{\mathrm{ev}}}{d}\right). \tag{7}$$

Thus, the shear rate in Eq. (5) scales as

$$\dot{\gamma} \sim \mathrm{O}\left(\frac{U_{\mathrm{ev}}}{d}\right). \tag{8}$$

The dynamic viscosity in Eq. (4) scales as

$$\mu\ \sim\ \mathrm{O}\left(K\left(\frac{U_{\mathrm{ev}}}{d}\right)^{n-1}\right), \tag{9}$$

which depends on the rheological parameters K and n. We can now obtain the order of rheology-dependent viscous force, f_v:

$$f_v = \nabla \cdot \{\mu[\nabla \boldsymbol{u} + (\nabla \boldsymbol{u})^T]\}\ \sim\ \mathrm{O}\left(\frac{1}{d}\,K\left(\frac{U_{\mathrm{ev}}}{d}\right)^{n-1}\frac{U_{\mathrm{ev}}}{d}\right)\ \sim\ \mathrm{O}\left(\frac{K}{d}\left(\frac{U_{\mathrm{ev}}}{d}\right)^{n}\right). \tag{10}$$

However, fluid rheology does not directly influence the distribution of ions. Thus, the order of electric body force, f_e, due to the net charge density in the diffusive interface can be scaled similarly to Newtonian fluids. The detailed scaling of f_e was presented by Chen *et al*. [28] and is omitted here:

$$f_e \sim\ \mathrm{O}\left(\Gamma\frac{\varepsilon E^2}{\delta}\right). \tag{11}$$

The order of electroviscous velocity can now be obtained by equating the viscous and electric forces, which gives

$$U_{\mathrm{ev}} \sim\ \mathrm{O}\left[d\left(\Gamma\frac{d}{\delta}\frac{\varepsilon E^2}{K}\right)^{1/n}\right]. \tag{12}$$

Combining Eqs. (1) and (12) gives the electric Rayleigh number in power-law fluids,

$$\mathrm{Ra}_{e,p-l} = \frac{hd}{D}\left(\Gamma\frac{d}{\delta}\frac{\varepsilon E^2}{K}\right)^{1/n}. \tag{13}$$

Note that for Newtonian fluids with $K = \mu$ and $n = 1$, Eq. (13) reduces to the same expression presented by Chen *et al*. [28], as shown in Eq. (1).

B. Approximation of local rheological parameters at the interface

To determine the electric Rayleigh number in power-law fluids, $\mathrm{Ra}_{e,p-l}$, we also need to obtain the effective diffusivity, D, and diffusion length, δ, of ions in Eq. (13). For the former, we can use the relationship [51]

$$D = D_0\frac{\mu_0}{\mu}, \tag{14}$$

where D_0 is the ion diffusivity in the Newtonian solvent with viscosity, μ_0. Estimating the local viscosity, μ, at the interface is challenging for our experiments because of the rheology mixing between Newtonian and shear thinning fluids. Therefore, it is important to have a good approximation of the local rheological parameters inside the mixing layer. Here we use a viscosity blending approach to estimate the power-law constants K and n at the interface by assuming a quasihomogeneous mixing of fluid rheology. Briefly, when two fluids with viscosities μ_1 and μ_2 mix, the viscosity of the resulting binary mixture can be approximated using the Arrhenius viscosity blending equation [59],

$$\mu = {\mu_1}^m \times {\mu_2}^{1-m}, \tag{15}$$

where m is the mole fraction of the fluid with viscosity μ_1. While more sophisticated models such as the Grunberg-Nissan [60] or Lederer-Roegiers [61,62] equations might offer higher accuracy, we choose the Arrhenius model due to its simplicity and convenience to use with the power-law constitutive relation. Plugging the shear-dependent viscosity in Eq. (4) yields

$$\mu \approx {K_1}^m\dot{\gamma}^{m(n_1-1)}{K_2}^{1-m}\dot{\gamma}^{(1-m)(n_2-1)}, \tag{16}$$

where K_1, n_1 and K_2, n_2 denote the power-law parameters of the corresponding fluids being mixed. If we assume equal contribution from both components at the interface, i.e., $m = 0.5$, the last equation can be rewritten as

$$\mu \approx \sqrt{K_1K_2}\,(\dot{\gamma})^{\frac{n_1+n_2}{2}-1} = K(\dot{\gamma})^{n-1}, \tag{17}$$

where $K = \sqrt{K_1K_2}$ and $n = (n_1 + n_2)/2$ are the local power-law constants of the rheology mixing at the interface. The ionic diffusion length, δ, in Eq. (13) for $\mathrm{Ra}_{e,p-l}$ is approximated by [29]

$$\delta \approx \sqrt{D\frac{L_x}{U_{\mathrm{eo}}}} = \sqrt{D_0\frac{\mu_0}{\mu}\frac{L_x}{U_{\mathrm{eo}}}}, \tag{18}$$

where L_x is the downstream location. Note that U_{eo} here is the electro-osmotic fluid velocity at the interface and can be estimated as $U_{\mathrm{eo}} = (\mu_{\mathrm{eo},1} + \mu_{\mathrm{eo},2})E/2$, with μ_{eo} being the experimentally measured electro-osmotic mobility of each fluid.

Since it is well established that the influence of polymer additives is generally much weaker in the bulk region than in the near-wall region (due to the velocity gradients) [43–45,63,64], one may question the validity of using bulk rheological parameters in our analysis rather than using the near-wall rheological parameters. In conventional electrokinetic flows with uniform electrolyte concentration, the velocity profile is typically pluglike, and velocity gradients are largely confined within the electric double layer, while the bulk flow remains nearly uniform and experiences negligible shear [1–4]. However, this study involves spatially varying ion concentrations across the channel, which generate substantial velocity gradients throughout the bulk electrolytes, especially

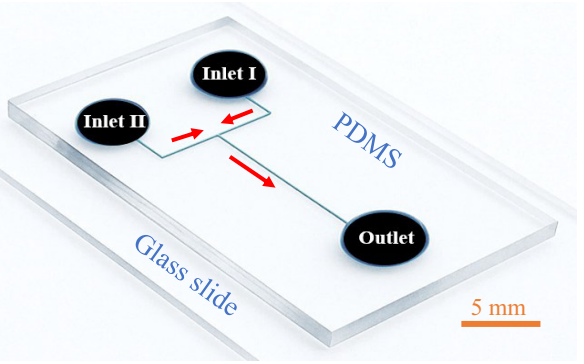

FIG. 1. Isometric view of the prepared T-shaped microchannel (filled with food dye for visualization) on which the arrows indicate the electrokinetic flow directions.

within the mixing layer. Consequently, it is reasonable to perform the analysis using the rheological properties at the mixing interface, where the EKI originates.

III. EXPERIMENT

A. Microchannel and fluids

We used a T-shaped microchannel fabricated through the standard soft-lithography technique with polydimethylsiloxane (PDMS). The detailed fabrication process has been reported in our earlier work [65]. As shown in Fig. 1, the prepared T-shaped microchannel features two side branches, each 8 mm long and 100 μm wide, and a main branch that is 10 mm long and 200 μm wide. The channel has a uniform depth of 50 μm. To minimize hydrostatic-pressure-driven backflow caused by electro-osmotic fluid depletion from the inlets and accumulation in the outlet, all reservoirs were made with a large 6-mm diameter. Before experiments, the microchannel was primed with deionized (DI) water (Fisher Scientific) for 10 min to ensure its walls retain uniform and constant surface properties.

We employed different fluid-pairing configurations to study how the direction of fluid rheology gradients interacts with conductivity gradients to influence EKI dynamics. Table I summarizes all the fluid configurations tested in our experiment. Specifically, the N/N (i.e., Newtonian/Newtonian) configuration with homogeneous rheology served as the control experiment and was designed as 0.2-mM and 2-mM Newtonian phosphate buffer (PB) solutions at inlets I and II of the microchannel (see Fig. 1), respectively. The 2-mM buffer was mixed with 50 μM rhodamine B dye (Sigma-Aldrich) for visualizing the interface. This concentration of rhodamine B dye has been reported to have negligible effects on the electro-osmotic flow of buffers for a pH range of 6–10.8 [66]. Two rheology mixing configurations, namely, N/ST (i.e., Newtonian/shear thinning) and ST/N (i.e., shear thinning/Newtonian) in Table I, involved pairing a Newtonian fluid with a shear thinning

TABLE I. Fluid pairing configurations in the experiment. The rhodamine B dye concentration was fixed at 50 μM in all cases. The abbreviations N and ST denote Newtonian and shear thinning fluids, respectively.

Configuration	Inlet I	Inlet II	Pairing type
N/N	0.2 mM PB	2 mM PB + dye	Homogeneous rheology
N/ST	0.2 mM PB + dye	2 mM PB + XG	Rheology mixing
ST/N	0.2 mM PB+ XG	2 mM PB + dye	Rheology mixing
ST/ST	0.2 mM PB + XG	2 mM PB + XG + dye	Homogeneous rheology

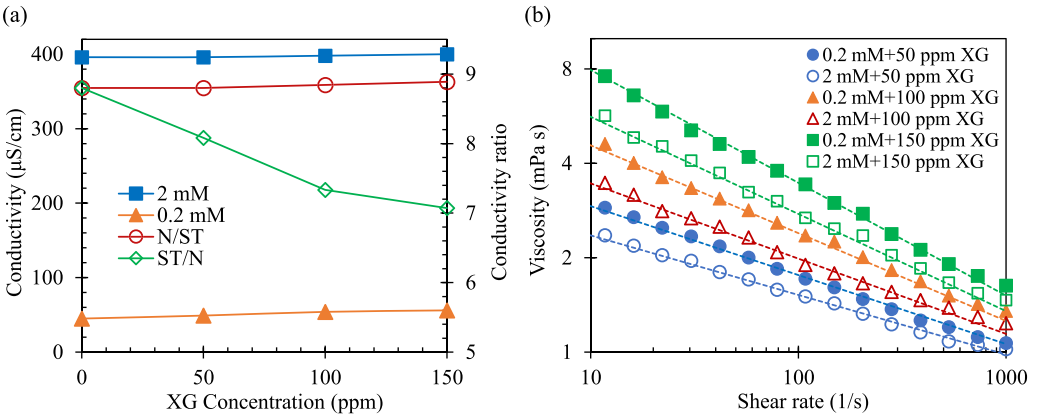

FIG. 2. Experimentally measured fluid properties: (a) electrical conductivities of 0.2- and 2-mM PB-based XG solutions and calculated conductivity ratios for the N/ST and ST/N fluid configurations (see Table I). The lines are used to guide the eyes only; (b) dynamic viscosities of 0.2-mM (filled markers) and 2-mM (hollow markers) PB-based XG solutions. The dotted lines represent the power-law fits to the experimental data points.

one. For the N/ST (ST/N) configuration, the shear thinning solution was prepared by adding 50–150 ppm XG polymer into 2-mM (0.2 mM) PB solution at inlet II (inlet I), while 0.2 mM (2 mM) dyed PB solution was used as the Newtonian fluid at inlet I (inlet II). The ST/ST configuration with homogeneous shear thinning rheology was tested in our previous study [51], where equal concentrations of XG polymer were added into 0.2-mM and 2-mM PB solutions, and selected results are used here for comparison.

Figure 2(a) shows the experimentally measured electrical conductivity, which increases slightly with increasing XG concentration in both 0.2-mM and 2-mM PB-based solutions. The conductivity ratio between the high- and low-concentration buffer solutions for the N/ST case remains almost identical, showing an insignificant increase from 8.80 to 8.89 when the XG concentration in 2 mM PB increases from 0 (i.e., the N/N configuration) to 150 ppm. In contrast, this ratio decreases from 8.80 at 0 ppm to 7.07 at 150 ppm by nearly 20% for the ST/N case when the XG concentration in 0.2 mM PB increases. These modifications in the conductivity ratio arise from the polymer-induced conductivity increase. We also tested a couple of dyed solutions, and the results showed no significant differences in conductivity compared to undyed solutions. Figure 2(b) shows the experimentally measured viscosities of 0.2- and 2-mM PB-based XG solutions, where the dotted lines are the power-law fits to the experimental data points. The dynamic viscosity was measured using a cone-plate rheometer (Anton Paar MCR 302) at room temperature. It shows an increasing trend at higher XG concentrations, with 2-mM PB-based solutions having lower viscosities compared to their 0.2-mM counterparts.

TABLE II. Power-law rheological parameters of PB-based XG solutions and inside the mixing layer for different fluid configurations. Note that the unit for the flow consistency index, K, is mPa s^n.

XG (ppm)	0.2 mM PB + XG		2 mM PB + XG		N/ST		ST/N		ST/ST	
	K	n	K	n	K	n	K	n	K	n
50	4.85	0.78	3.65	0.81	1.91	0.91	2.20	0.89	4.21	0.80
100	8.70	0.72	6.00	0.76	2.45	0.88	2.95	0.86	7.22	0.74
150	18.2	0.64	11.5	0.69	3.39	0.85	4.27	0.82	14.5	0.67

Table II lists the flow consistency index, K, and power-law index, n, obtained from the power-law fits. The latter quantity, $n \leqslant 1$, reflects the degree of shear thinning, with lower values indicating stronger shear thinning behavior. One can thus notice that the shear thinning behavior becomes more pronounced with increasing XG concentration and is comparatively stronger in 0.2-mM PB-based solutions. Table II also lists the calculated power-law constants of the mixing layer for the three fluid configurations (i.e., N/ST, ST/N, and ST/ST) via Eq. (17). The K and n values are each comparable in between the N/ST and ST/N configurations, while K is the largest, i.e., most viscous, and n is the smallest, i.e., most shear thinning, in the ST/ST configuration. It is important to note that our prepared XG solutions are assumed to be purely shear thinning with a negligible elasticity effect as previously reported [67,68]. This assumption enables the use of the power-law model in the theoretical formulation above (Sec. II). The analysis of the influence of fluid elasticity and hence normal stress differences on EKI will be considered in future work.

B. Visualization and measurements

After priming, the DI water was emptied from all reservoirs of the T-shaped microchannel. Equal volumes of prepared fluids were added to the two inlet reservoirs according to the fluid configuration being tested. The outlet reservoir was filled with the same volume of 0.2-mM pure buffer to eliminate any pressure-driven flow. Platinum electrodes were then inserted into all three reservoirs, with the two inlet electrodes being connected in parallel to a dc power source (Glassman High Voltage) while the outlet electrode was grounded. This setup ensured equal dc electric fields across the side branches, driving the electro-osmotic flow toward the outlet. The applied electric field was limited to a maximum of 500 V/cm (corresponding to 900-V dc potential across the 1.8-cm overall channel length) to avoid gel formation [69] and Joule heating effects [25]. The interface dynamics was recorded from a top-down view using a fluorescent microscope (Nikon Eclipse TE2000U) with a Nikon DS-Qi1 monochrome CCD camera. Image acquisition was carried out at around 12 frames per second with 70-ms exposure time.

The captured images were processed using Nikon's imaging software (NIS Elements AR 2.30) to quantify the properties of EKI waves. The wave speed was measured by tracking the valley of individual waves over time. The wave amplitude was defined as half of the average distance from valley to peak and normalized by half-width of the main branch. The wave frequency was determined by counting the number of peaks in intensity plots over a time span of 20 s. The electro-osmotic velocity, U_{eo}, was measured using a 2-cm-long, straight microchannel through the electric current monitoring technique [70]. The microchannel for this measurement was primed similarly to the T-shaped microchannel used in the EKI experiment. The electro-osmotic mobility, $\mu_{\mathrm{eo}} = U_{\mathrm{eo}}/E$, was obtained from a linear fit to the experimental data of U_{eo} vs electric field. This linear electro-osmosis has been demonstrated in our previous study for low-concentration XG solutions [51]. As seen from Fig. 3, μ_{eo} is larger in 0.2-mM PB-based XG solutions than in 2-mM PB, both of which decrease with increasing XG concentration. These values were used to calculate U_{eo} inside the mixing layer at the threshold electric field and in turn the critical electric Rayleigh number, $\mathrm{Ra}_{e,p-l,\mathrm{cr}}$, for the onset of EKI in different fluid configurations.

IV. RESULTS AND DISCUSSION

A. Effects of rheology mixing on EKI

Figure 4 compares the experimental images of EKI waves in the two rheology mixing configurations, i.e., N/ST and ST/N, and the N/N fluid configuration (see Table I). The XG concentration was fixed at 50 ppm. Compared to the N/N case, EKI triggers at significantly lower threshold electric fields, E_{th}, in the N/ST and ST/N configurations. This observation is consistent with our previous study in the ST/ST configuration, which was attributed to the enhancement effect of fluid shear thinning on EKI [51]. The measured $E_{\mathrm{th}} = 183$ V/cm for the N/ST configuration is nearly 20% smaller than the threshold value of 222 V/cm for the ST/N configuration. This phenomenon

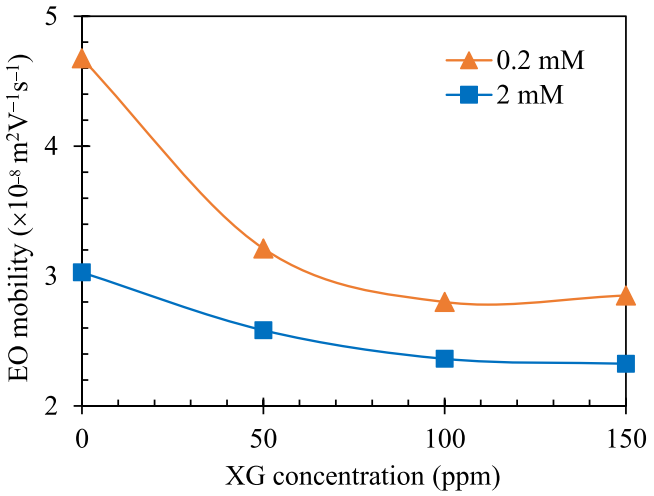

FIG. 3. Experimentally measured electro-osmotic (EO) mobilities, U_{eo}/E, of 0.2-mM and 2-mM PB-based XG solutions. The lines are used to guide the eyes only.

suggests that there are other factors contributing to EKI because the fluid in the mixing layer of the N/ST configuration is in fact slightly less shear thinning than the ST/N configuration (see Table II). A similar trend to E_{th} is also noticed for the downstream locations where EKI waves first emerge (pointed to by the arrows on the images in Fig. 4). In the N/N case, the EKI waves originate furthest downstream and progressively shift upstream with increasing electric fields. In contrast, they originate much closer to the stagnation point in the two mixing configurations, with the N/ST configuration initiating waves directly at the stagnation point. Moreover, as seen from the images, the EKI waves in each configuration become visually stronger when the applied electric field increases beyond the corresponding threshold. However, the wave amplitudes in the two mixing configurations are noticeably smaller than in the N/N configuration under the same electric field.

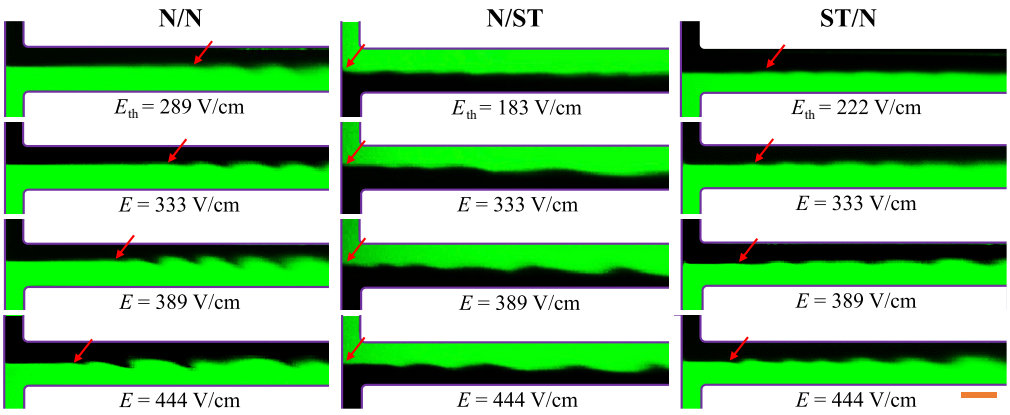

FIG. 4. Comparison of the EKI images at the T-junction for the N/N (left), N/ST (middle), and ST/N (right) fluid configurations at varying electric fields. The XG concentration in the N/ST and ST/N cases was fixed at 50 ppm. E_{th} refers to the threshold electric field for the onset of EKI waves. The arrows point to the downstream locations where EKI waves first appear. The scale bar indicates 200 μm.

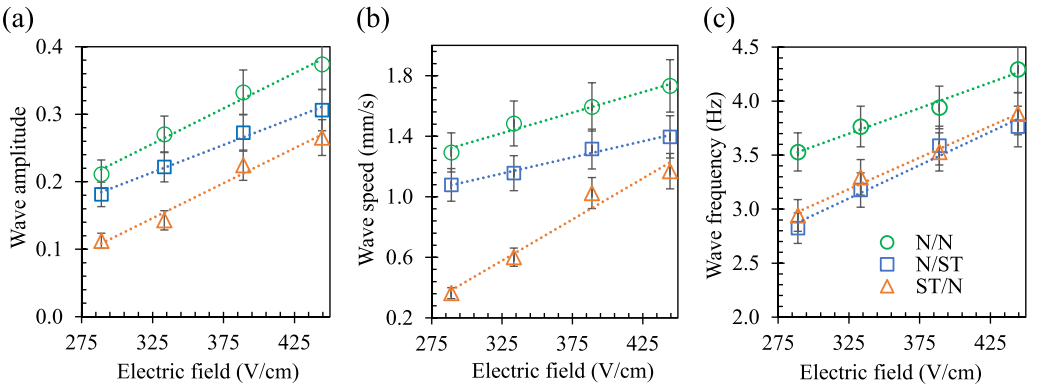

FIG. 5. Comparison of experimentally measured amplitude (a, relative to the half-width of the main branch), speed (b), and frequency of EKI waves in the N/N, N/ST, and ST/N fluid configurations at varying electric fields. The dotted lines represent linear fits to the data points.

Figure 5 compares the measured speeds, amplitudes, and frequencies of EKI waves among the three fluid configurations at various above-threshold electric fields. We see a linear increasing trend of wave properties with electric fields in all configurations, similar to the ST/ST configuration in our previous study [51]. At any given electric fields, the two rheology mixing configurations both exhibit weaker wave responses than the N/N case. This observation is also consistent with our previous findings in the ST/ST configuration, which may be attributed to the polymer-induced viscous damping [51,52]. In particular, the N/ST configuration shows higher wave amplitudes in Fig. 5(a) and speeds in Fig. 5(b) than the ST/N configuration because of the smaller fluid viscosity in the mixing layer for the former case (see Table II). Interestingly, the temporal frequencies in Fig. 5(c) remain nearly identical in the two mixing configurations, though they are both smaller than that in the N/N case under every electric field. The reasons for this invariance are currently unclear to the authors and require numerical investigations.

As it also exhibits the lowest E_{th} for the onset of EKI, the N/ST configuration appears to yield stronger EKI responses compared to ST/N because of the competition of the following four factors present in the definition of electric Rayleigh number, $\text{Ra}_{e,p\text{-}l}$, in Eq. (13): (1) shear thinning in terms of the power-law index n: a smaller n (i.e., more shear thinning) increases $\text{Ra}_{e,p-l}$, leading to enhanced EKI in the ST/N configuration; (2) conductivity gradient in terms of Γ: a smaller Γ decreases $\text{Ra}_{e,p-l}$, leading to diminished EKI in the ST/N configuration; (3) viscous damping in terms of fluid viscosity μ, involved in the ion diffusivity D in Eq. (14) and diffusion length δ in Eq. (18): a larger μ reduces both D and δ, thus increasing $\text{Ra}_{e,p-l}$, leading to enhanced EKI in the ST/N configuration; (4) electro-osmotic convection in terms of U_{eo} involved in the diffusion length δ: a smaller U_{eo} decreases $\text{Ra}_{e,p-l}$, leading to diminished EKI in the ST/N configuration. A direct comparison of $\text{Ra}_{e,p-l}$ between the two rheology mixing configurations will be provided in the next section.

B. Effects of polymer concentration on critical conditions for EKI

Figure 6(a) presents the experimental images of EKI waves in the N/ST and ST/N fluid configurations with varying XG concentrations under their respective threshold electric fields, E_{th}. These images reveal two key trends: one is that E_{th} is lower in the N/ST configuration compared to ST/N for all XG concentrations, and the other is that E_{th} decreases with higher polymer concentration in both configurations. In addition, the onset location of EKI waves in the N/ST configuration remains at the stagnation point, while that in the ST/N configuration shifts upstream toward the stagnation point with increasing XG concentration. Both trends are consistent with those observed

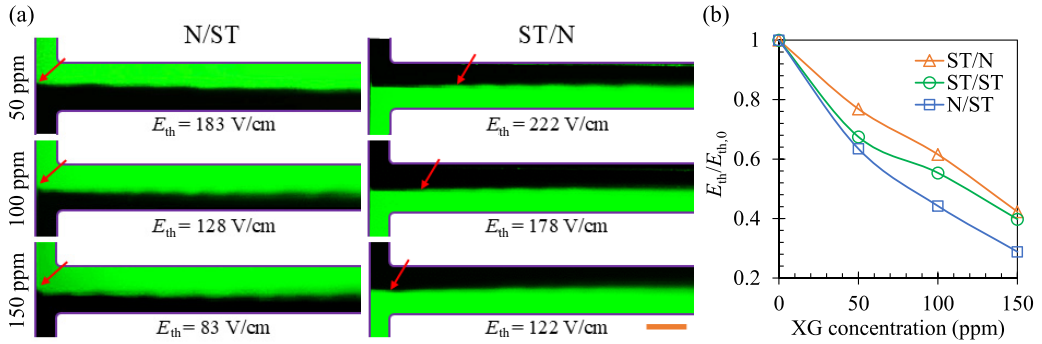

FIG. 6. (a) Experimental images of EKI waves under threshold electric fields, E_{th}, in the N/ST (left) and ST/N (right) fluid configurations with varying XG concentrations. The arrows on the images point to the onset location of EKI waves, and the scale bar indicates 200 μm. (b) Comparison of E_{th} (normalized by $E_{th,0}$ for the N/N configuration in Fig. 4) among the N/ST, ST/N, and ST/ST [51] configurations.

in Fig. 4 against the applied electric field. Figure 6(b) compares the values of E_{th} (normalized by $E_{th,0}$ for the N/N configuration in Fig. 4) in between the N/ST and ST/N fluid configurations, along with those in the ST/ST configuration from our previous work [51]. The threshold fields in the homogeneous rheology configuration, i.e., ST/ST, lie between those of rheology mixing configurations. This phenomenon suggests that EKI is enhanced over homogeneous shear thinning fluids when the gradients of shear thinning rheology and electrical conductivity are in the same direction. The opposite happens if the rheology gradient is introduced in the opposite direction of the conductivity gradient. In other words, the rheology gradient itself may be able to induce instability in electrokinetic microchannel flows, which will be our future work.

Figure 7(a) compares the critical electric Rayleigh numbers, $\mathrm{Ra}_{e,\mathrm{cr}}$ (normalized by $Ra_{e,\mathrm{cr},0}$ in the N/N fluid configuration), for the onset of EKI in the three fluid configurations, which were calculated via the formulation in Eq. (2) from our previous work [51]. One can see that $\mathrm{Ra}_{e,\mathrm{cr}} < 1$ in XG solutions, regardless of the fluid configuration, further validating the statement in our previous

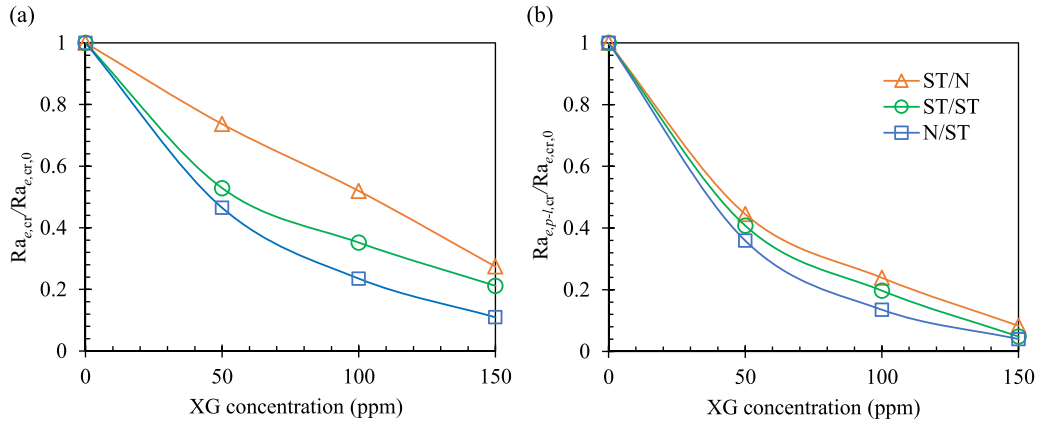

FIG. 7. Comparison of the critical electric Rayleigh numbers (normalized by $\mathrm{Ra}_{e,\mathrm{cr},0}$ in the N/N fluid configuration) for the onset of EKI waves among the N/ST, ST/N, and ST/ST configurations: (a) $\mathrm{Ra}_{e,\mathrm{cr}}$ via the formulation in Eq. (2) from our previous work [51]; (b) $\mathrm{Ra}_{e,p-l,\mathrm{cr}}$ via the formulation in Eq. (13) from this work. The curves for the ST/ST configuration are plotted using the experimental data of threshold electric fields from our previous work [51]. All lines are used to guide the eyes only.

work that the addition of shear thinning XG polymer enhances EKI [51]. Moreover, $\mathrm{Ra}_{e,\mathrm{cr}}$ decreases continuously with increasing XG concentration in each fluid configuration and exhibits similar variations across the fluid configurations to E_{th} in Fig. 6(b). Specifically, the N/ST configuration shows the lowest $\mathrm{Ra}_{e,\mathrm{cr}}$, and the ST/ST configuration remains in the middle over the range of XG concentrations. As an example, at 100-ppm XG concentration, the ST/N configuration shows a ratio of $\mathrm{Ra}_{e,\mathrm{cr}}/\mathrm{Ra}_{e,\mathrm{cr},0} = 0.52$, roughly 120% higher than that in the N/ST configuration, which is only 0.24. Meanwhile, the ST/ST configuration yields a ratio of 0.35, positioned midway between the other two. Like E_{th} in Fig. 6(b), such trend of $\mathrm{Ra}_{e,\mathrm{cr}}$ across the fluid configurations also suggests the impact of fluid rheology gradient on EKI in microchannel flows.

As noted in the Introduction, our previous formulation of Eq. (2) [51] did not consider the fluid rheology effects on $\mathrm{Ra}_{e,\mathrm{cr}}$. Therefore, the obtained $\mathrm{Ra}_{e,\mathrm{cr}}/\mathrm{Ra}_{e,\mathrm{cr},0} < 1$ in Fig. 7(a) for all cases is essentially a result of the XG polymer-addition-induced variations in fluid viscosity, electro-osmotic velocity, and conductivity, excluding shear thinning rheology. Here, we further calculated the critical electric Rayleigh numbers in power-law fluids via $\mathrm{Ra}_{e,p-l}$ in Eq. (13) for each fluid configuration with varying XG concentrations at the corresponding E_{th}. Specifically, we used Eq. (18) to calculate the ion diffusion length, δ, at $L_x = 1.5$ mm downstream location, which is approximately the length of the main branch in the recorded experimental images. The fluid viscosity was set to $\mu_0 = 1.0 \times 10^{-3}\,\mathrm{kg\,m^{-1}\,s^{-1}}$ for both 0.2- and 2-mM PB solutions, in which the ion diffusivity was assumed to be $D_0 = 1.0 \times 10^{-9}\,\mathrm{m^2\,s^{-1}}$ [28]. The electro-osmotic velocity, U_{eo}, in Eq. (18) was approximated as the average electro-osmotic fluid velocity at the interface, which was calculated from $U_{\mathrm{eo}} = (\mu_{\mathrm{eo},1} + \mu_{\mathrm{eo},2})E_{\mathrm{th}}/2$, with $\mu_{\mathrm{eo},1}$ and $\mu_{\mathrm{eo},2}$ being the experimentally measured electro-osmotic mobilities of the two fluids (see Fig. 3). To determine the local fluid viscosity at the interface, i.e., μ in Eqs. (14) and (18), we first estimated the local shear rate via $\dot{\gamma} = 2U_{\mathrm{eo}}/h$. The dynamic viscosity was then calculated using Eq. (17), where the power-law constants K and n in each fluid configuration are presented in Table II.

Figure 7(b) compares the values of $\mathrm{Ra}_{e,p-l,\mathrm{cr}}$ among the three shear thinning fluid configurations, which are also normalized by $\mathrm{Ra}_{e,\mathrm{cr},0}$ in the N/N fluid configuration for consistency with $\mathrm{Ra}_{e,\mathrm{cr}}$ in Fig. 7(a). Similar variations to $\mathrm{Ra}_{e,\mathrm{cr}}$ are observed for $\mathrm{Ra}_{e,p-l,\mathrm{cr}}$, both across the fluid configurations and over the XG concentrations. However, the gaps in $\mathrm{Ra}_{e,p-l,\mathrm{cr}}$ among the three configurations are noticeably smaller than those in $\mathrm{Ra}_{e,\mathrm{cr}}$. As an example, for 100-ppm XG concentration, the ST/ST configuration shows a ratio of $\mathrm{Ra}_{e,p-l,\mathrm{cr}}/\mathrm{Ra}_{e,\mathrm{cr},0} = 0.20$. This value is about 40% higher than that in the N/ST configuration, which is 0.14, while almost 20% lower than the ST/N configuration, which is 0.24. This difference between $\mathrm{Ra}_{e,\mathrm{cr}}$ in Fig. 7(a) and $\mathrm{Ra}_{e,p-l,\mathrm{cr}}$ in Fig. 7(b) highlights the modifications by fluid-rheology-induced viscous stress in the electric Rayleigh number formulation. Moreover, the observation that $\mathrm{Ra}_{e,p-l,\mathrm{cr}}$ is smaller than the corresponding $Ra_{e,\mathrm{cr}}$ in all fluid configurations under every XG concentration indicates the enhancement effect of fluid shear thinning on EKI. This is further to the enhancement effect of polymer-addition-induced fluid viscosity, conductivity, and electro-osmotic velocity variations as reflected by $\mathrm{Ra}_{e,\mathrm{cr}}$ in Fig. 7(a).

A natural question is whether our electric Rayleigh number analysis based on the power-law model will remain valid if a more realistic constitutive model, such as the Carreau model [58], is adopted for the fluid shear thinning effect. The Carreau model predicts a finite viscosity plateau at both low and high shear rates, with an intermediate regime in which the viscosity follows a power-law-type decay. In contrast, the power-law model represents only an approximation of the intermediate shear regime and does not capture the plateau behavior. It is, however, important to note that the estimated local shear rates (approximated via $\dot{\gamma} = 2U_{\mathrm{eo}}/h$) in our experiments fall within the power-law regime. For example, in the 50-ppm N/ST configuration, the shear rate varies from approximately 13 $\mathrm{s^{-1}}$ at the threshold electric field to 32 $\mathrm{s^{-1}}$ at the maximum applied electric field of 444 V/cm. As evident from Fig. 2(b), this range of shear rates lies within the power-law decay region. Hence, our analysis should remain valid even if a more realistic shear thinning fluid model is used instead of the power-law model.

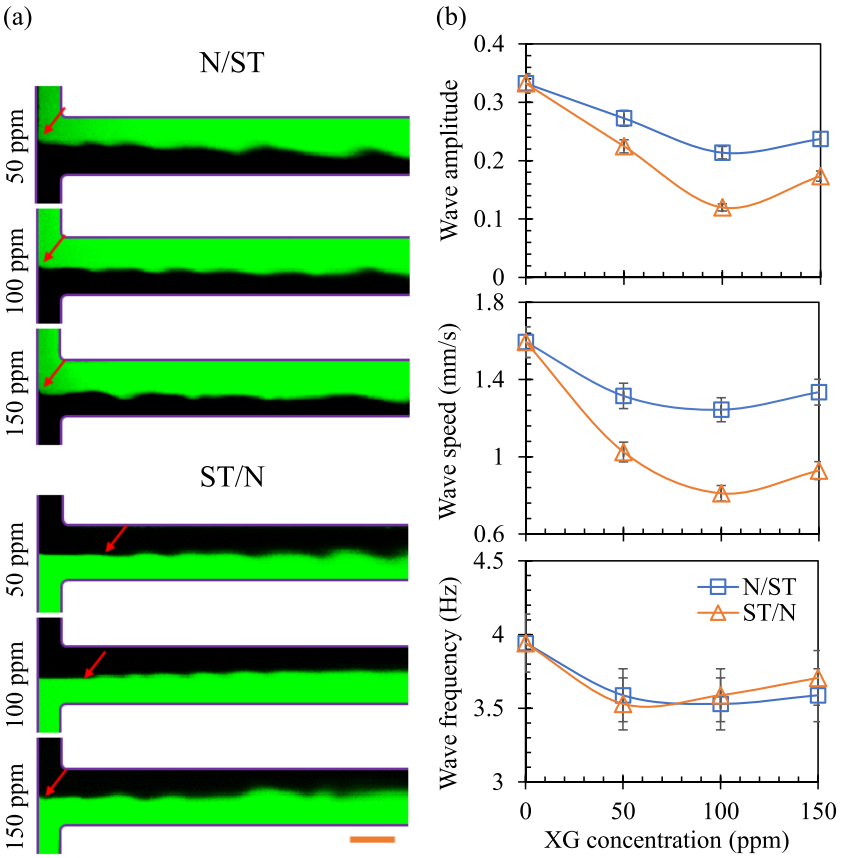

FIG. 8. Comparison of EKI waves in the N/ST and ST/N fluid configurations with varying XG concentrations under a fixed electric field of 389 V/cm: (a) experimental images, where the arrows point to the onset location of EKI waves and the scale bar indicates 200 μm; (b) experimentally measured wave amplitude (top), speed (middle), and frequency (bottom), where all lines are used to guide the eyes only.

C. Effects of polymer concentration on EKI wave properties

Figure 8(a) presents the experimental images of EKI waves in the N/ST and ST/N fluid configurations with varying XG concentrations. One can see that under a fixed electric field of 389 V/cm, the wave amplitude first decreases from 50 to 100 ppm XG concentration and then increases again at 150 ppm in both configurations. This nonmonotonic behavior is confirmed by the quantitative plot of wave amplitude against XG concentration in Fig. 8(b) (top). It is consistent with our previous study of EKI in the ST/ST fluid configuration [51], which results from the combined effects of polymer-addition-induced variations in fluid viscosity, shear thinning behavior, electro-osmotic velocity, and conductivity ratio. The N/ST configuration has a higher wave amplitude than the ST/N configuration for all nonzero XG concentrations, which aligns with the observation in Fig. 5(a) and may be partially associated with the larger viscosity of the latter (see Table II). Figure 8(b) also presents the experimentally measured speed (middle) and frequency (bottom) of EKI waves in the N/ST and ST/N configurations. These two properties exhibit a similar nonmonotonic trend to the wave amplitude in both configurations. Like that in Fig. 5(b), the N/ST configuration has higher wave speeds than the ST/N configuration because of the viscosity difference. In contrast, the wave frequencies in the two configurations remain almost identical, supporting our observation in

Fig. 5(c). Further studies, especially numerical [71,72], are needed to fully understand the EKI in microchannel flows with both conductivity and rheology gradients.

V. CONCLUSIONS

We have investigated the effects of fluid rheology gradients on EKI using a T-shaped microchannel. Our experiment demonstrates that introducing shear thinning XG polymer into either the high- (i.e., N/ST fluid configuration) or low- (i.e., ST/N fluid configuration) conductivity PB solution enhances EKI by reducing the threshold electric field required for instability. However, the extent of this enhancement varies with the direction of the rheology gradient. Adding XG to the high-conductivity buffer in the N/ST configuration results in more pronounced EKI characteristics with higher wave speeds, greater amplitudes, and lower threshold electric fields, compared to XG in the lower-conductivity buffer of the ST/N configuration. These observations suggest that EKI is enhanced when the shear thinning rheology and conductivity gradients are in the same direction. Moreover, the gradient of shear thinning alone may be able to induce instability in electrokinetic flows. The threshold electric fields in the homogeneous ST/ST fluid configuration are found to be in between those for the two rheology mixing configurations across the XG concentrations. To further examine the critical conditions for the onset of EKI, we have also revised the scaling analysis of Chen *et al.*'s electric Rayleigh number formulation [28] to account for the fluid shear thinning effects on EKI. The critical values of this power-law fluid–based dimensionless number exhibit similar variations to the threshold electric field across both the fluid configurations and XG concentrations. Our analysis suggests that the observed variations in EKI behaviors among the fluid configurations stem from the differences in rheological properties of the mixing layer. These findings deepen our understanding of how fluid rheology gradients influence EKI in microfluidic systems, offering valuable insights into designing microfluidic devices that require precise control over fluid mixing and particle manipulation. In future work we will investigate the effects of other non-Newtonian rheology (such as viscoelasticity) gradients on EKI.

ACKNOWLEDGMENTS

This work was supported in part by NASA under Grant No. 80NSSC24M0173 (Y.X. and X.X.), by the NSF under Grants No. CBET-2100772 and No. CBET- 2127825 (X.X.), and by Clemson University through the Creative Inquiry Program (X.X.).

M.M.I., S.M.T., N.M., Y.L., and A.S. performed the experiment; M.M.I. conducted the theoretical analysis; M.M.I. and S.M.T. analyzed the experimental data; J.B.B., Y.X., and X.X. supervised the project; X.X. designed the project; M.M.I. wrote the manuscript; J.B.B., Y.X., and X.X. edited the manuscript; all authors commented on the manuscript.

DATA AVAILABILITY

The data that support the findings of this article are not publicly available. The data are available from the authors upon reasonable request.

[1] C. Zhao and C. Yang, Advances in electrokinetics and their applications in micro/nano fluidics, Microfluid. Nanofluid. **13**, 179 (2012).

[2] B. H. Lapizco-Encinas, Recent developments in the use of electrokinetic methods for rapid cell viability assessments and separations, J. Chromatogr. Open **6**, 100185 (2024).

[3] G. M. Whitesides and A. D. Stroock, Flexible methods for microfluidics, Phys. Today **54**(6), 42 (2001).

[4] X. Xuan, Recent advances in direct current electrokinetic manipulation of particles for microfluidic applications, Electrophoresis **40**, 2484 (2019).
[5] B. Saha, S. Chowdhury, S. Sarkar, and P. P. Gopmandal, Electroosmotic flow modulation and dispersion of uncharged solutes in soft nanochannel, Soft Matter **20**, 6458 (2024).
[6] M. R. Hossan, D. Dutta, N. Islam, and P. Dutta, Review: Electric field driven pumping in microfluidic device, Electrophoresis **39**, 702 (2018).
[7] I. Rubinstein and B. Zaltzman, Electroconvection in electrodeposition: Electrokinetic regularization mechanisms of shortwave instabilities, Phys. Rev. Fluids **9**, 053701 (2024).
[8] S. K. Mehta and P. K. Mondal, Electroosmotic mixing of viscoplastic fluids in a microchannel, Phys. Rev. Fluids **9**, 023301 (2024).
[9] S. Ghosal, Electrokinetic flow and dispersion in capillary electrophoresis, Annu. Rev. Fluid Mech. **38**, 309 (2006).
[10] Y. Huang and M. Wang, Solvent mixing and ion partitioning effects in spontaneous charging and electrokinetic flow of immiscible liquid-liquid interface, Phys. Rev. Fluids **9**, 103701 (2024).
[11] H. Zhao, X. Xuan, and N. Wu, Concentration polarization induced electro-osmosis around a charged dielectric microchannel corner, Phys. Rev. Fluids **10**, 044203 (2025).
[12] J. R. Melcher and G. I. Taylor, Electrohydrodynamics: A review of the role of interfacial shear stresses, Annu. Rev. Fluid Mech. **1**, 111 (1969).
[13] C. Sasmal, Electro-elastic instability and turbulence in electro-osmotic flows of viscoelastic fluids: Current status and future directions, Micromachines **16**, 187 (2025).
[14] H. Lin, Electrokinetic instability in microchannel flows: A review, Mech. Res. Commun. **36**, 33 (2009).
[15] R. Bharadwaj and J. G. Santiago, Dynamics of field-amplified sample stacking, J. Fluid Mech. **543**, 57 (2005).
[16] M. A. Saucedo-Espinosa and B. H. Lapizco-Encinas, Refinement of current monitoring methodology for electroosmotic flow assessment under low ionic strength conditions, Biomicrofluid. **10**, 033104 (2016).
[17] Y. Song, D. Li, and X. Xuan, Recent advances in multimode microfluidic separation of particles and cells, Electrophoresis **44**, 910 (2023).
[18] K. Dubey, S. Sanghi, A. Gupta, and S. S. Bahga, Electrokinetic instability due to streamwise conductivity gradients in microchip electrophoresis, J. Fluid Mech. **925**, A14 (2021).
[19] J. Park, S. M. Shin, K. Y. Huh, and I. S. Kang, Application of electrokinetic instability for enhanced mixing in various micro–T-channel geometries, Phys. Fluids **17**, 118101 (2005).
[20] C. H. Tai, R. J. Yang, M. Z. Huang, C. W. Liu, C. H. Tsai, and L. M. Fu, Micromixer utilizing electrokinetic instability-induced shedding effect, Electrophoresis **27**, 4982 (2006).
[21] J. D. Posner, C. L. Pérez, and J. G. Santiago, Electric fields yield chaos in microflows, Proc. Natl Acad. Sci. USA **109**, 14353 (2012).
[22] M. Z. Huang, R. J. Yang, C. H. Tai, C. H. Tsai, and L. M. Fu, Application of electrokinetic instability flow for enhanced micromixing in cross-shaped microchannel, Biomed. Microdev. **8**, 309 (2006).
[23] D. A. Boy and B. D. Storey, Electrohydrodynamic instabilities in microchannels with time periodic forcing, Phys. Rev. E **76**, 026304 (2007).
[24] W. J. Luo, Effect of ionic concentration on electrokinetic instability in a crossshaped microchannel, Microfluid. Nanofluid. **6**, 189 (2009).
[25] L. Song, L. Yu, C. Brumme, R. Shaw, C. Zhang, and X. Xuan, Joule heating effects on electrokinetic flows with conductivity gradients, Electrophoresis **42**, 967 (2021).
[26] P. Gupta and S. Singh Bahga, Mechanism of sinuous and varicose modes in electrokinetic instability, Phys. Rev. E **110**, 035106 (2024).
[27] P. Gupta and S. Singh Bahga, Lorenz model for chaos in electrokinetic instability, Electrophoresis **46**, 912 (2025).
[28] C.-H. Chen, H. Lin, S. K. Lele, and J. G. Santiago, Convective and absolute electrokinetic instability with conductivity gradients, J. Fluid Mech. **524**, 263 (2005).
[29] J. D. Posner and J. G. Santiago, Convective instability of electrokinetic flows in a cross-shaped microchannel, J. Fluid Mech. **555**, 1 (2006).

[30] H. Lin, B. D. Storey, and J. G. Santiago, A depth-averaged electrokinetic flow model for shallow microchannels, J. Fluid Mech. **608**, 43 (2008).
[31] J. F. Hoburg and J. R. Melcher, Internal electrohydrodynamic instability and mixing of fluids with orthogonal field and conductivity gradients, J. Fluid Mech. **73**, 333 (1976).
[32] J. C. Baygents and F. Baldessari, Electrohydrodynamic instability in a thin fluid layer with an electrical conductivity gradient, Phys. Fluids **10**, 301 (1998).
[33] H. Lin, B. D. Storey, M. H. Oddy, C.-H. Chen, and J. G. Santiago, Instability of electrokinetic microchannel flows with conductivity gradients, Phys. Fluids **16**, 1922 (2004).
[34] B. D. Storey, B. S. Tilley, H. Lin, and J. G. Santiago, Electrokinetic instabilities in thin microchannels, Phys. Fluids **17**, 018103 (2005).
[35] M. H. Oddy and J. G. Santiago, Multiple-species model for electrokinetic instability, Phys. Fluids **17**, 064108 (2005).
[36] C. Zhao and C. Yang, Electrokinetics of non-Newtonian fluids: A review, Adv. Colloid Interface Sci. **201–202**, 94 (2013).
[37] X. Lu, C. Liu, G. Hu, and X. Xuan, Particle manipulations in non-Newtonian microfluidics: A review, J. Colloid Interface Sci. **500**, 182 (2017).
[38] F. Pimenta and M. A. Alves, Electro-elastic instabilities in cross-shaped microchannels, J. Non-Newtonian Fluid Mech. **259**, 61 (2018).
[39] C. A. Browne, A. Shih, and S. S. Datta, Pore-scale flow characterization of polymer solutions in microfluidic porous media, Small **16**, 1903944 (2020).
[40] M. K. Raihan, N. Kim, Y. Song, and X. Xuan, Elasto-inertial instabilities in the merging flow of viscoelastic fluids, Soft Matter **20**, 6059 (2024).
[41] S. S. Datta, A. M. Ardekani, P. E. Arratia, A. N. Beris, I. Bischofberger, G. H. McKinley, J. G. Eggers, J. Esteban López-Aguilar, S. M. Fielding, A. Frishman, M. D. Graham, J. S. Guasto, S. J. Haward, A. Q. Shen, S. Hormozi, A. Morozov, R. J. Poole, V. Shankar, E. S. G. Shaqfeh, H. Stark, *et al.*, Perspectives on viscoelastic flow instabilities and elastic turbulence, Phys. Rev. Fluids **7**, 080701 (2022).
[42] C. Sasmal, Potential applications of elastic instability and elastic turbulence: A comprehensive review, limitations, and future directions, J. Non-Newtonian Fluid Mech. **337**, 105393 (2025).
[43] S. Wei, Z. Cheng, P. Nath, M. D. Tikekar, G. Li, and L. A. Archer, Stabilizing electrochemical interfaces in viscoelastic liquid electrolytes, Sci. Adv. **4**, eaao6243 (2018).
[44] M. D. Tikekar, G. Li, L. A. Archer, and D. L. Koch, Electroconvection and morphological instabilities in potentiostatic electrodeposition across liquid electrolytes with polymer additives, J. Electrochem. Soc. **165**, A3697 (2018).
[45] G. Li, L. A. Archer, and D. L. Koch, Electroconvection in a viscoelastic electrolyte, Phys. Rev. Lett. **122**, 124501 (2019).
[46] D.-L. Chen, Y. Xie, C. Yang, G. Liu, Z. Li, F. Liu, and H.-L. Yi, A polymer-based strategy for regulating electroconvective instability and ion transport at ion-selective membranes, J. Membrane Sci. **739**, 124901 (2026).
[47] S. Maurya, M. Trivedi, and N. Nirmalkar, Influence of shear-thinning rheology on electroconvection around ion-selective membrane, J. Non-Newtonian Fluid Mech. **348**, 105545 (2026).
[48] L. Song, P. P. Jagdale, L. Yu, Z. Liu, D. Li, C. Zhang, and X. Xuan, Electrokinetic instability in microchannel viscoelastic fluid flows with conductivity gradients, Phys. Fluids **31**, 082001 (2019).
[49] C. Sasmal, Fluid viscoelasticity suppresses chaotic convection and mixing due to electrokinetic instability, Phys. Fluids **34**, 082011 (2022).
[50] F. Hamid and C. Sasmal, Strong effect of fluid rheology on electrokinetic instability and subsequent mixing phenomena in a microfluidic T-junction, Phys. Fluids **35**, 013107 (2023).
[51] T. Chen, M. K. Raihan, S. M. Tabarhoseini, C. Gabbard, M. M. Islam, Y. Lee, J. Bostwick, L. Fu, and X. Xuan, Electrokinetic flow instabilities in shear thinning fluids with conductivity gradients, Soft Matter **21**, 699 (2025).
[52] T. Chen, M. M. Islam, C. Gabbard, Y. Lee, M. K. Raihan, J. Bostwick, L. Fu, and X. Xuan, Electrokinetic instabilities in Boger fluid flows with conductivity gradients, Phys. Fluids **37**, 062016 (2025).
[53] P. J. Cullen, *Food Mixing: Principles and Applications* (John Wiley & Sons, New York, 2009).

[54] T. Hoare, D. Zurakowski, R. Langer, and D. S. Kohane, Rheological blends for drug delivery. I. Characterization in vitro, J. Biomed. Mater. Res. A **92A**, 575 (2010).
[55] E. Karavas, E. Georgarakis, and D. Bikiaris, Application of PVP/HPMC miscible blends with enhanced mucoadhesive properties for adjusting drug release in predictable pulsatile chronotherapeutics, Eur. J. Pharm. Biopharm. **64**, 115 (2006).
[56] H. Klok, Biological–synthetic hybrid block copolymers: Combining the best from two worlds, J. Polym. Sci. **43**, 1 (2005).
[57] W. J. Frith, Mixed biopolymer aqueous solutions – Phase behaviour and rheology, Adv. Colloid Interface Sci. **161**, 48 (2010).
[58] R. B. Bird, R. C. Armstrong, and O. Hassager, *Dynamics of Polymeric Liquids* (Wiley-Interscience, Hoboken, NJ, 1987), Vol. 1.
[59] B. Zhmud, Viscosity blending equations, Lube Magazine **121**, 24 (2014).
[60] L. Grunberg and A. H. Nissan, The energies of vaporisation, viscosity and cohesion and the structure of liquids, Trans. Faraday Soc. **45**, 125 (1949).
[61] E. L. Lederer, Zur Theorie der Viskosität von Flüssigkeiten, Kolloid-Beih. **34**, 270 (1931).
[62] M. Roegiers, Discussion of the fundamental equation of viscosity, Scientific Lubrication **3**, 27 (1951).
[63] C. M. White and M. G. Mungal, Mechanics and prediction of turbulent drag reduction with polymer additives, Annu. Rev. Fluid Mech. **40**, 235 (2008).
[64] J.-P. Cheng, H.-N. Zhang, W.-H. Cai, S.-N. Li, and F.-C. Li, Effect of polymer additives on heat transport and large-scale circulation in turbulent Rayleigh-Bénard convection, Phys. Rev. E **96**, 013111 (2017).
[65] D. T. Kumar, Y. Zhou, V. Brown, X. Lu, A. Kale, L. Yu, and X. Xuan, Electric field-driven instabilities in ferrofluid microflows, Microfluid. Nanofluid. **19**, 43 (2015).
[66] K. F. Schrum, J. M. Lancaster, S. E. Johnston, and S. D. Gilman, Monitoring electroosmotic flow by periodic photobleaching of a dilute, neutral fluorophore, Anal. Chem. **72**, 4317 (2000).
[67] A. Lindner, D. Bonn, and J. Meunier, Viscous fingering in a shear-thinning fluid, Phys. Fluids **12**, 256 (2000).
[68] M. Aytouna, J. Paredes, N. Shahidzadeh-Bonn, S. Moulinet, C. Wagner, Y. Amarouchene, J. Eggers, and D. Bonn, Drop formation in non-Newtonian fluids, Phys. Rev. Lett. **110**, 034501 (2013).
[69] C. H. Ko, D. Li, A. Malekanfard, Y. Wang, L. Fu, and X. Xuan, Electroosmotic flow of non-Newtonian fluids in a constriction microchannel, Electrophoresis **40**, 1387 (2019).
[70] A. Sze, D. Erickson, L. Ren, and D. Li, Zeta-potential measurement using the Smoluchowski equation and the slope of the current–time relationship in electroosmotic flow, J. Colloid Interface Sci. **261**, 402 (2003).
[71] A. M. Afonso, F. T. Pinho, and M. A. Alves, Electro-osmosis of viscoelastic fluids and prediction of electro-elastic flow instabilities in a cross slot using a finite-volume method, J. Non-Newtonian Fluid Mech. **179–180**, 55 (2012).
[72] M. A. Alves, P. J. Oliveira, and F. T. Pinho, Numerical methods for viscoelastic fluid flows, Annu. Rev. Fluid Mech. **53**, 509 (2021).